

Cite this: *J. Mater. Chem. A*, 2021, 9, 10796

Unprecedentedly high efficiency for photocatalytic conversion of methane to methanol over Au–Pd/TiO₂ – what is the role of each component in the system?†

Xiaojiao Cai,^a Siyuan Fang^b and Yun Hang Hu *^b

Direct and highly efficient conversion of methane to methanol under mild conditions still remains a great challenge. Here, we report that Au–Pd/TiO₂ could directly catalyze the conversion of methane to methanol with an unprecedentedly high methanol yield of 12.6 mmol g_{cat}^{−1} in a one-hour photocatalytic reaction in the presence of oxygen and water. Such an impressive efficiency is contributed by several factors, including the affinity between Au–Pd nanoparticles and intermediate species, the photothermal effect induced by visible light absorption of Au–Pd nanoparticles, the employment of O₂ as a mild oxidant, and the effective dissolution of methanol in water. More importantly, for the first time, thermo-photo catalysis is demonstrated by the distinct roles of light. Namely, UV light is absorbed by TiO₂ to excite charge carriers, while visible light is absorbed by Au–Pd nanoparticles to increase the temperature of the catalyst, which further enhances the driving force of corresponding redox reactions. These results not only provide a valuable guide for designing a photocatalytic system to realize highly efficient production of methanol, but also, highlight the great promise of thermo-photo catalysis.

Received 15th January 2021
Accepted 31st March 2021

DOI: 10.1039/d1ta00420d

rsc.li/materials-a

Introduction

Methane, as the main constituent of natural gas, has been widely used as a gaseous fuel and an important raw material to produce methanol, hydrogen, acetylene, *etc.*^{1,2} Conversion of methane to methanol is especially desired and has been regarded as the holy grail reaction in C1 chemistry because methanol is an essential feedstock in the chemical and energy industries. This can be achieved either directly or indirectly *via* syngas or methyl esters with catalysts.^{3,4} Direct conversion in the gas phase generally requires a high temperature (200–500 °C) to activate the oxidant and accelerate the desorption of as-generated methanol, whereas overoxidation generally occurs.^{5–7} This can be effectively addressed by carrying out the catalytic reaction in the liquid phase with hydrogen peroxide (H₂O₂) as the oxidant.^{6,7} However, the cost of H₂O₂ is even higher than those of the oxygenated products, making this process uneconomical.⁸ Direct utilization of O₂ to convert methane to methanol under mild conditions still remains a huge challenge.

Other than traditional thermal catalysis, photocatalysis shows great promise for molecular activation due to the facile production of free radicals.⁹ So far, TiO₂, ZnO, WO₃, BiVO₄, Bi₂WO₆, black phosphorus, *etc.* have been employed as semiconductor photocatalysts for methane conversion.^{5,10–16} However, bare semiconductors generally show poor photocatalytic activities due to the fast recombination of photo-generated charge carriers, which can be suppressed by loading appropriate cocatalysts.^{5,14,17,18} The cocatalysts exploited for photocatalytic methane conversion include metals such as Pt, Pd, Au, and Ag,^{5,19} and metal oxides such as FeO_x, CoO_x, and Ag₂O.^{14,20,21} However, currently reported methanol production rates are in the range from 2 to 4300 μmol g_{cat}^{−1} h^{−1} (Table S1†), which are far below the requirement for scalable production. This encourages us to explore multi-component cocatalysts such as alloys where the synergetic effect of different components is expected.

Alloy cocatalysts can promote photocatalysis by extending the light absorption range,²² balancing the distribution of electron density,²³ enhancing interfacial charge transfer kinetics,²⁴ providing distinct active sites for redox reactions,²⁵ *etc.* Au, as an excellent electronic conductor, can facilitate the transfer of photo-excited electrons, and more importantly, hinders the oxidation of other coupling metals such as Ag, Ni, Pd, and Cu during photocatalysis as Au is less oxophilic.²⁶ Pd is an ideal candidate to couple with Au because Pd can not only strongly absorb both UV and visible light *via* inter-band

^aSchool of Environmental Science and Engineering, Shanghai Jiao Tong University, Shanghai 200240, People's Republic of China^bDepartment of Materials Science and Engineering, Michigan Technological University, Houghton, Michigan 49931-1295, USA. E-mail: yunhangh@mtu.edu

† Electronic supplementary information (ESI) available. See DOI: 10.1039/d1ta00420d

electronic transitions but also effectively trap photo-excited electrons.^{27,28} So far, Au–Pd containing catalysts have been studied mainly in photocatalytic hydrogen production^{23,27,28} and pollutant degradation,²⁹ whereas their application in photocatalytic methane conversion has not been explored yet.

Furthermore, the plasmon resonance absorption of noble metal nanoparticles (NPs) is well known to induce the photo-thermal effect, which results in a locally high temperature.³⁰ This leads to a unique thermo-photo catalytic system without additional thermal energy. In our previous studies, with the simultaneous supply of thermal and photo energies *via* a furnace and lamp, photocatalytic efficiency was found to be significantly enhanced because thermal energy could increase the driving force for photocatalytic reactions and thereby break the kinetic limitations in photocatalysis.^{2,31–36} However, thermo-photo catalysis under mild conditions without any external heat source has not been explored yet. Here, the Au–Pd containing system is ideal for studying this kind of thermo-photo catalysis due to the notable photothermal effect.

In this work, we synthesized a Au–Pd/TiO₂ catalyst *via* a sol-immobilization method and conducted photocatalytic methane conversion over it in the presence of oxygen and water. Impressively, an unprecedentedly high methanol yield of 12.6 mmol g_{cat}^{−1} was obtained in just one hour. This is due to the affinity between Au–Pd NPs and CH₃OOH which is beneficial for its further conversion, the synergetic effect of thermal and photo energies realized by visible light absorption by Au–Pd NPs and UV light absorption by TiO₂, the employment of O₂ as a mild oxidant, and the efficient dissolution of the oxygenated products by water. Furthermore, the reaction mechanism was proposed.

Experimental

Materials

Hydrogen tetrachloroaurate trihydrate (HAuCl₄·3H₂O, ≥99.0% Au basis, Sigma-Aldrich) and palladium chloride (PdCl₂, ≥99.9%, Sigma-Aldrich) were used as metal precursors. Commercial titanium dioxide (submicron TiO₂, ≥99.9%, Shanghai Macklin Biochemical Co., Ltd) was used as the catalyst support. Sodium borohydride (NaBH₄, 99.99%, Sigma-Aldrich) and polyvinyl pyrrolidone (PVP, MW = 1 300 000, Sigma-Aldrich) were used as the reducing agent and stabilizer for catalyst preparation, respectively. Methane (99.999%, Air Liquide Shanghai Co., Ltd) and oxygen (99.999%, Air Liquide Shanghai Co., Ltd) were used as the feedstock gases. Hydrogen peroxide (H₂O₂, 3.0 wt%, Sigma-Aldrich) was used for comparison. Double-distilled water was used in all experiments.

Catalyst preparation

1 wt% Au–Pd/TiO₂ (atomic ratio of Au and Pd = 1) was prepared using a sol-immobilization method. 1.08 mL HAuCl₄ aqueous solution (59 mM) and 3.2 mL PdCl₂ aqueous solution (20 mM in 0.5 M HCl) were dissolved simultaneously in 800 mL distilled water to give a precursory solution containing 0.08 mM Au³⁺ and 0.08 mM Pd²⁺. 0.023 g PVP was then added to the solution.

After 2–3 min of stirring, 6.4 mL freshly prepared 0.1 M NaBH₄ aqueous solution was added twice such that the molar ratio of NaBH₄-to-metal was 5.0. The produced dark-brown colloid was stirred for 30 min to ensure all the metal precursors were reduced to the metallic form. Afterwards, the colloid was immobilized by adding 2.0 g TiO₂ under vigorous stirring, followed by quick acidification to pH = 1 with 1 M sulfuric acid to achieve more homogeneous deposition of metal NPs. The supernatant became clear after 1 h, indicating that the deposition process was complete. The sol-immobilized catalyst was then filtered and washed thoroughly with 2.0 L distilled water and dried at 110 °C for 16 h. Monometallic catalysts containing Au or Pd NPs and metal-free catalysts were prepared following the same procedure but with a single metal precursor or without metal precursors. The total mole number of decorated metal(s) was kept the same for bimetallic and monometallic catalysts.

Catalyst characterization

The crystal structure of the samples was determined in air by using an X-ray diffractometer (Bruker/Siemens D5000 system) with a Cu K α radiation source ($\lambda = 1.54056 \text{ \AA}$) in the range from 10 to 80° and a step size of 2° min^{−1}. The morphology of the samples was investigated by using a high-resolution transmission electron microscope (HR-TEM) (FEI Tecnai G2 F20) equipped with a Gatan digital camera operated at an acceleration potential of 200 kV with a FEG field effect. The optical properties of the samples were recorded by using a UV-visible absorption spectrophotometer (Shimadzu UV-2550), scanning from 200 to 1400 nm with two detection shifts at 300 and 900 nm, respectively. Steady-state photoluminescence spectra were obtained using a Varian Cary-Eclipse 500 spectrometer with an excitation wavelength at 380 nm. The chemical state of the samples was analyzed using an X-ray photoelectron spectrometer (Thermo Fisher 250Xi) with a full-spectrum pass energy of 100 eV and a step size of 0.6 eV at a 15 kV acceleration voltage. All binding energies were calibrated with respect to the C1s line of surface adventitious carbon at 284.8 eV. Electron paramagnetic resonance (EPR) spectra were recorded on a Bruker Elexsys E500 spectrometer with 2,2-dimethyl-3,4-dihydro-2H-pyrrole-1-oxide (DMPO) as the spin probe. Mott-Schottky measurements were conducted in a three-electrode cell in 0.5 M Na₂SO₄ solution in the dark, where the catalyst-coated fluorine-doped tin oxide glass, Pt, and saturated calomel served as the working, counter, and reference electrodes, respectively.

Photocatalytic conversion of methane

Methane conversion was carried out in a 100 mL stainless steel autoclave reactor with a Teflon vessel, gas inlet and outlet, and a quartz window on the top for light irradiation. A xenon lamp with full-spectrum irradiation was employed as the light source and the light intensity was controlled at 250 mW cm^{−2}. To investigate the respective roles of UV and visible light, a UV reflector and a UV filter were employed for UV and visible light irradiation, respectively, with 425 nm as the cutoff wavelength. The light intensities of UV and visible light were 91 and 165 mW

cm^{-2} , respectively. The temperature of the suspension was measured using a thermocouple placed in the reactor. The reactor can be heated by using an electric furnace.

In a typical test, 5 mg catalyst and 30 mL distilled water were added into the reactor. Then the autoclave was sealed and purged with oxygen three times, followed by pressurization with 3.0 MPa methane and 1.0 MPa oxygen. Prior to the photocatalytic reaction, the suspension was magnetically stirred at 1000 rpm in the dark for 20 min to reach the adsorption-desorption equilibrium. The reaction lasted for 1 h under stirring. After reaction, the autoclave reactor was cooled in ice to a temperature below 10 °C to minimize the loss of volatile products. Then, CO and CO₂ were quantified by using a gas chromatograph (GC) equipped with a thermal conductive detector and a TDX-01 column. Subsequently, the aqueous mixture was filtered for analysis. CH₃OH was analyzed by GC with a flame ionization detector and a Porapak Q packed column. CH₂O was measured by acetylacetonone spectrophotometry at 413 nm. CH₃OOH and HCOOH were quantified by high-performance liquid chromatography (HPLC) with a 250 m C18 column.

Results and discussion

Catalyst characterization

Au/TiO₂, Pd/TiO₂, and Au-Pd/TiO₂ were prepared *via* a sol-immobilization approach. TiO₂ existed in the anatase form as demonstrated by XRD patterns (Fig. S1†), while no diffraction peaks corresponding to Au and Pd were detected, which might be caused by their high dispersion and low concentration. According to TEM images, metal NPs were well dispersed on TiO₂ (Fig. 1a–c). Au NPs in Au/TiO₂ and Pd NPs in Pd/TiO₂ were found to have an average size of 2.65 ± 0.87 and 4.91 ± 1.37 nm, respectively, while the mean size of Au-Pd NPs in Au-Pd/TiO₂ was ~ 3.8 nm. The small and uniform size of metal NPs could enhance the separation of photo-generated charges and supply more active sites. Moreover, the obtained Au-Pd NPs exhibited lattice spacings of 0.235 and 0.225 nm, which were consistent with those of Au(200) and Pd(111) planes as observed in Au/TiO₂ and Pd/TiO₂, demonstrating the formation of a polycrystalline Au-Pd alloy.³⁷ Furthermore, element mapping (Fig. 1d) revealed that the distribution of Au agreed well with that of Pd, especially for relatively large NPs. This kind of alloy-like structure enabled effective interaction between the two metals and TiO₂, thus forming both metal-metal and metal-titania heterojunctions.

To reveal the electronic interactions and chemical states of the samples, XPS analysis was performed. O1s XPS spectra (Fig. 2a) could be deconvoluted into three peaks, corresponding to lattice oxygen (O_L), surface hydroxyl (O_H), and absorbed water (O_W), respectively.^{38,39} The proportion of O_H reached the highest (14.53%) in Au-Pd/TiO₂ among these catalysts (Table S2†), which would contribute to ·OH production. Ti³⁺ was not found in the surface layer of all the samples (Fig. 2b). Moreover, compared with the monometallic counterparts, Au-Pd/TiO₂ showed a slightly promoted oxidation of Au but a significantly inhibited oxidation of Pd (Fig. 2c and d). The binding energies of both metallic Au and Pd shifted to lower values, indicating the accelerated charge transfer

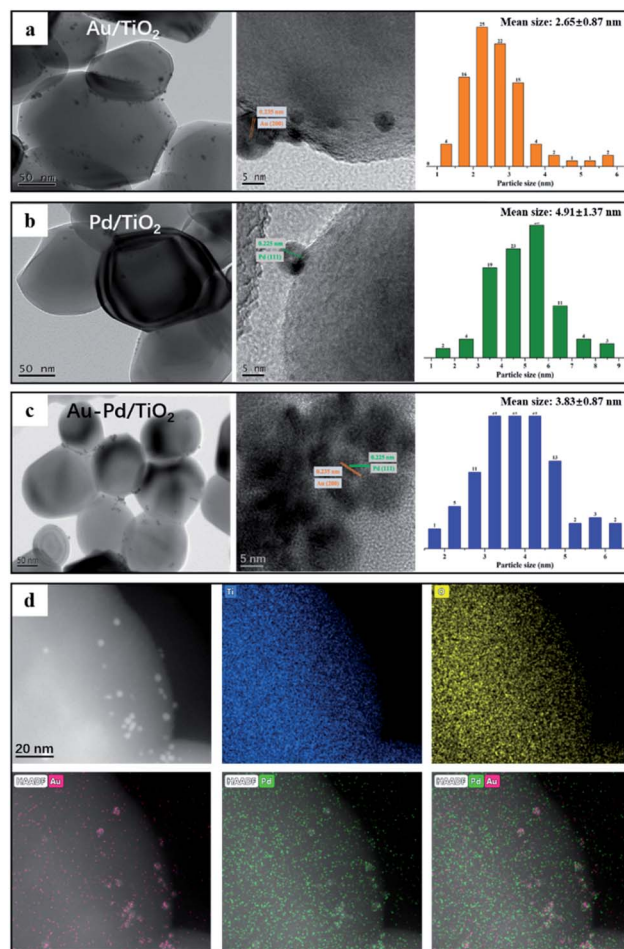


Fig. 1 TEM images and corresponding size distributions of metal NPs in (a) Au/TiO₂, (b) Pd/TiO₂, and (c) Au-Pd/TiO₂. (d) Elemental maps of Au-Pd/TiO₂.

from TiO₂ to metal NPs, which would be beneficial for multiple-electron reduction to produce oxygenates.

Furthermore, the optical properties of the catalysts were comparatively analysed. The UV-visible spectrum of Au-Pd/TiO₂ showed strong visible light absorption but without the characteristic Au plasmon absorption peak at ~ 530 nm (Fig. 3a), which indicated a strong interaction between Au and Pd and further implied the formation of a Au-Pd alloy. Moreover, there was no significant difference in the band gaps of these catalysts (~ 3.18 eV), revealing that TiO₂ and metal NPs were responsible for UV and visible light absorption, respectively. The photoluminescence (PL) spectra are shown in Fig. 3b, where the photoluminescence intensity decreased in the order of TiO₂ > Au-Pd/TiO₂ > Pd/TiO₂ > Au/TiO₂, suggesting the easier recombination of the charge carriers in Au-Pd/TiO₂ compared with Au/TiO₂ and Pd/TiO₂.

Activity comparison between Au-Pd/TiO₂ and its monometallic counterparts

Photocatalytic methane oxidation was carried out in a batch reactor with a quartz window on the top for light irradiation.

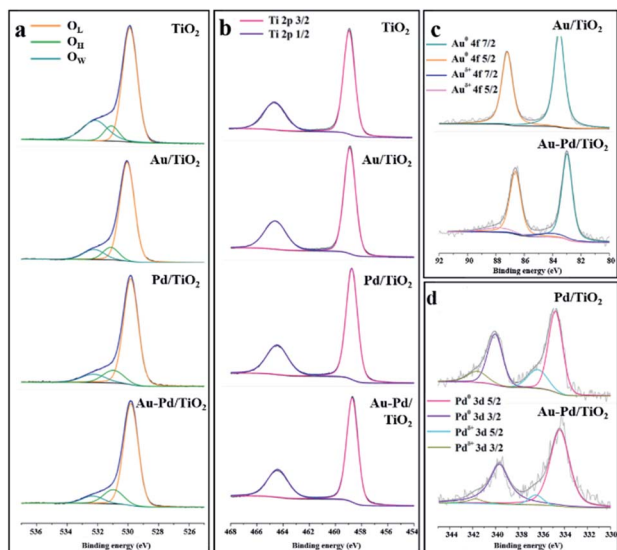


Fig. 2 XPS spectra of bare TiO₂, Au/TiO₂, Pd/TiO₂, and Au–Pd/TiO₂. (a) Ti 2p, (b) O 1s, (c) Au 4f, and (d) Pd 3d XPS spectra.

5 mg catalyst was suspended in 30 mL water and the reaction took place under vigorous magnetic stirring in the presence of 3.0 MPa CH₄ and 1.0 MPa O₂ for one hour. Under sunlight irradiation (UV-visible light, 250 mW cm⁻²), all the catalysts, namely, TiO₂, Au/TiO₂, Pd/TiO₂, and Au–Pd/TiO₂, showed excellent photocatalytic activities with large amounts of CH₃OOH, CH₃OH, and CH₂O detected, together with scarce amounts of HCOOH, CO, and CO₂ (Fig. 4). The selectivity of the total liquid oxygenates even reached 98% for all the catalysts. The total yields obtained over TiO₂, Au/TiO₂, Pd/TiO₂, and Au–Pd/TiO₂ were 12.4, 20.8, 30.8, and 20.0 mmol g⁻¹, respectively. The relatively low methane conversion efficiency over Au–Pd/TiO₂ was attributed to the high recombination rate of charge carriers as demonstrated by the PL spectra (Fig. 3b).

However, though Au/TiO₂ and Pd/TiO₂ could convert methane more efficiently, the dominant product was CH₃OOH with high selectivities of 60.1% and 66.0%, which was just an intermediate species in methane conversion with limited value.⁵ In other words, further conversion of CH₃OOH to CH₃OH, CH₂O, and other products with higher oxidation degrees was suppressed over Au/TiO₂ and Pd/TiO₂. In contrast, over Au–Pd/TiO₂, an impressive CH₃OH yield of 8.6 mmol g⁻¹

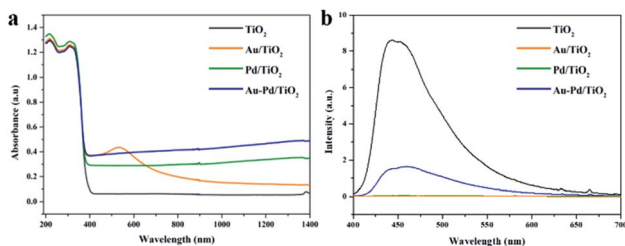


Fig. 3 Optical properties of TiO₂, Au/TiO₂, Pd/TiO₂, and Au–Pd/TiO₂. (a) UV-visible diffuse reflectance spectra. (b) Photoluminescence spectra.

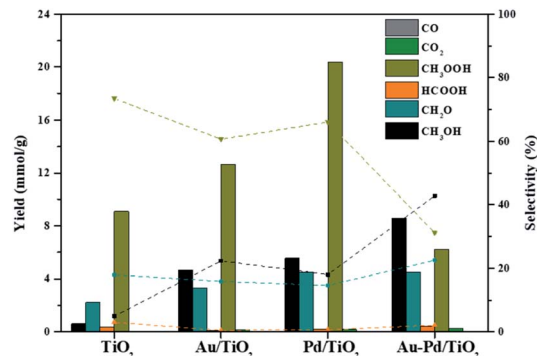


Fig. 4 Photocatalytic methane oxidation over TiO₂, Au/TiO₂, Pd/TiO₂, and Au–Pd/TiO₂ under UV-visible light irradiation (5 mg catalyst, 30 mL water, 3.0 MPa CH₄, 1.0 MPa O₂, 1 h reaction).

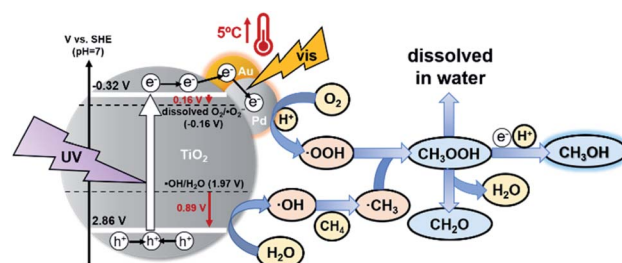
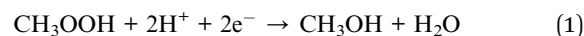


Fig. 5 Reaction mechanism of photocatalytic methane conversion over Au–Pd/TiO₂.

and a high selectivity of 42.8% were obtained, in great contrast to those of 0.6 mmol g⁻¹ and 4.9% over TiO₂, 4.6 mmol g⁻¹ and 22.3% over Au/TiO₂, and 5.6 mmol g⁻¹ and 18.0% over Pd/TiO₂ (Fig. 4). In general, there are three destinies of as-produced CH₃OOH on the catalyst surface: (1) being reduced to CH₃OH (eqn (1)), (2) being oxidized to CH₂O (eqn (2)), and (3) dissolving in water (Fig. 5).^{5,20}



The affinity between CH₃OOH and Au–Pd NPs was beneficial for its further conversion compared with dissolution, and the abundant electrons on Au–Pd NPs (demonstrated by XPS and PL spectra) promoted the reduction of CH₃OOH to CH₃OH. This was further evidenced by measuring the activities of Au–Pd/TiO₂ catalysts with various Au–Pd loading amounts (Fig. S2†). Namely, the increased Au–Pd loading amount led to the decrease of the selectivity for CH₃OOH while increasing the selectivity for CH₃OH. Furthermore, TEM images revealed that there was no evident difference in the sizes of Au–Pd NPs in samples with different loading amounts, while the quantity of Au–Pd NPs increased with the loading amount (Fig. S3†). This implied that more Au–Pd NPs could provide more active sites for the conversion of CH₃OOH to CH₃OH. Based on these

results, Au–Pd/TiO₂ was considered as an ideal catalyst for highly efficient methane conversion to CH₃OH.

The role of UV and visible light

In order to clarify the respective roles of UV and visible light, which were mainly absorbed by TiO₂ and Au–Pd NPs respectively, photocatalytic methane conversion was carried out under individual UV (91 mW cm⁻²) and visible (165 mW cm⁻²) light irradiation with the water temperature fixed at the same temperature as that under full-spectrum illumination (42 °C). It is interesting that though visible light itself made little contribution to methane conversion, the addition of visible light to UV light evidently promoted the production of all products, especially CH₃OH, whose yield increased from 6.2 to 8.6 mmol g⁻¹ (Fig. 6). Herein, as-absorbed visible light by Au–Pd NPs could provide additional heat for the catalyst due to the photothermal effect.⁴⁰ As an indirect approach to measuring the temperature of the catalyst, we respectively dispersed Au–Pd/TiO₂, Au/TiO₂, and Pd/TiO₂ onto a SiO₂ substrate, heated them to 42 °C, turned on the light, and then measured their temperature by thermocoupling after 15 min stabilization. It was clearly found that visible light irradiation could induce an evident thermal effect during the illumination period from 15 to 60 min (Table 1). The addition of visible light to UV light led to an ~5 °C temperature rise of the Au–Pd/TiO₂ and Pd/TiO₂ catalysts, while the Au/TiO₂ catalyst showed a much more significant increase of the temperature to ~12 °C. This implied that Au was the main contributor to the photothermal effect, owing to its localized surface plasmon resonance, whereas this could be suppressed to some extent by forming an alloy.

That is to say, in this case, the absorption of UV light by TiO₂ was responsible for the excitation of charge carriers to drive corresponding reactions, while visible light absorbed by Au–Pd NPs could provide heat to accelerate these reactions. This leads to a unique process of thermo-photo catalysis realized by the synergetic effects of UV and visible light. In order to elucidate this unique process, the band structure of Au–Pd/TiO₂ was depicted based on the Mott–Schottky plot (Fig. S4†) and UV-visible spectrum (Fig. 3a). Moreover, active species were

Table 1 Temperature of the catalyst coated on a SiO₂ substrate under UV, visible, and UV-visible light irradiation (background temperature: 42 °C, presented temperature: the average temperature during the illumination period from 15 to 60 min)

Substance	UV	Visible	UV-visible
SiO ₂	44.8 °C	45.3 °C	45.1 °C
Au/TiO ₂ on SiO ₂	43.7 °C	55.8 °C	56.0 °C
Pd/TiO ₂ on SiO ₂	45.0 °C	49.3 °C	50.1 °C
Au–Pd/TiO ₂ on SiO ₂	47.5 °C	51.7 °C	52.3 °C

revealed *via* EPR measurements of the catalyst suspension with 5,5-dimethyl-1-pyrroline N-oxide (DMPO) as the spin probe. As shown in Fig. S5,† the co-existence of ·OH and ·O₂⁻ was demonstrated over Au–Pd/TiO₂ under light irradiation since the DMPO–OH spin adduct (with a quartet EPR signal) and the DMPO–OOH spin adduct (with a sextet EPR signal) were detected.⁴¹ This indicated the processes of O₂ reduction to ·O₂⁻ by photo-excited electrons and H₂O (or surface hydroxyl) oxidation to ·OH by photo-excited holes. The generation of ·OH could promote the activation of C–H bonds, during which Au played an important role due to its strong electron-accepting ability.⁴²

Based on the above observations, the oxidation driving force (energy difference between the redox potential of ·OH/H₂O (ref. 43) and the valence band maximum) was found to be 0.89 V, while the reduction driving force (energy difference between the conduction band minimum and the redox potential of dissolved O₂/·O₂⁻ (ref. 44)) was even as small as 0.16 V (Fig. 5). As revealed in our previous work, insufficient potential driving force would suppress the photocatalytic reaction.^{31–34} Here, the heat resulting from the photothermal effect could make the reactants adsorbed on the catalyst more active, enhancing the kinetic driving force and thus promoting photocatalysis. Moreover, the more notable promotion in the production of CH₃OH than that of other products might be because the ~5 °C temperature rise showed more significant contribution to electron donation from the conduction band of TiO₂ through Au–Pd NPs to CH₃OOH to form CH₃OH (eqn (1)) by enhancing its driving force. This is the first time we demonstrate thermo-photo catalysis achieved by the distinct roles of light.

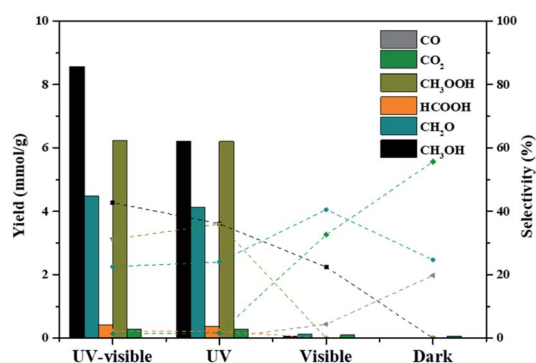


Fig. 6 Photocatalytic methane oxidation over Au–Pd/TiO₂ under UV-visible, UV, and visible light irradiation with the water temperature controlled at 42 °C (5 mg catalyst, 30 mL water, 3.0 MPa CH₄, 1.0 MPa O₂, 1 h reaction).

The role of oxidants

Furthermore, the role of oxidants was comparatively investigated (Fig. 7). In the absence of O₂ and H₂O₂, 5.1 mmol g⁻¹ CH₃OOH was generated as the dominant product. In this case, water itself and/or dissolved O₂ served as the oxidant, leading to a mild oxidation process. Adding 10 mM H₂O₂ into water mainly promoted the further conversion of CH₃OOH into CH₃OH (1.2 mmol g⁻¹), CH₂O (3.0 mmol g⁻¹), and HCOOH (4.0 mmol g⁻¹), while the total yield showed a slight enhancement from 6.3 to 9.1 mmol g⁻¹. The selectivity of CH₃OH was as low as 13.3%. In contrast, introducing 1.0 MPa O₂ which possesses a weaker oxidizing ability than H₂O₂ was advantageous for the production of CH₃OOH (6.2 mmol g⁻¹), CH₃OH (8.6 mmol g⁻¹), and CH₂O (4.5 mmol g⁻¹), with a scarce amount of HCOOH

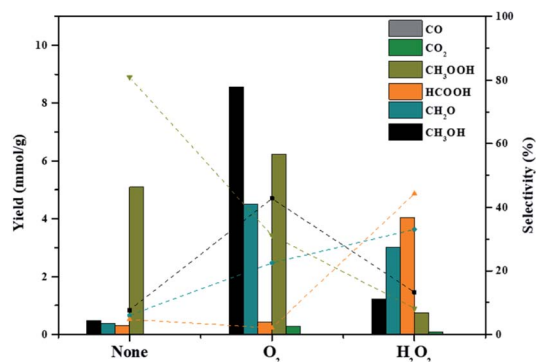


Fig. 7 Photocatalytic methane oxidation over Au–Pd/TiO₂ without or with O₂ or H₂O₂ under UV-visible light irradiation (5 mg catalyst, 30 mL water, 3.0 MPa CH₄, 10 mM H₂O₂ or 1.0 MPa O₂, 1 h reaction).

(0.4 mmol g⁻¹). Besides, the total yield was significantly enhanced by more than three fold from 6.3 to 20.0 mmol g⁻¹. In terms of CH₃OH production, the selectivity and productivity obtained with O₂ were 3 and 7 times those with H₂O₂. From this perspective, the use of O₂ rather than H₂O₂ was not only cost-effective but also highly-efficient for CH₃OH production.

The role of water

Moreover, it is of vital importance to investigate the role of water in photocatalytic methane conversion. As shown in Fig. 8, the yield of CH₃OH (mmol g⁻¹) significantly increased by four fold, from 3.3 to 12.6 mmol g⁻¹, with the increase of the water volume from 10 to 50 mL. Here, the water volume could not be further increased due to the limitation of the reactor. Nevertheless, such a remarkable yield is three times higher than the highest value reported so far (Table S1†). In contrast to the rapid increase of the yield, the concentration of CH₃OH (mmol L⁻¹) showed slight reduction with water volume. The above observations implied that water was an effective solvent for CH₃OH and there was a balance between the adsorbed and dissolved CH₃OH. Therefore, more water was beneficial for obtaining more CH₃OH. A similar phenomenon was also observed in

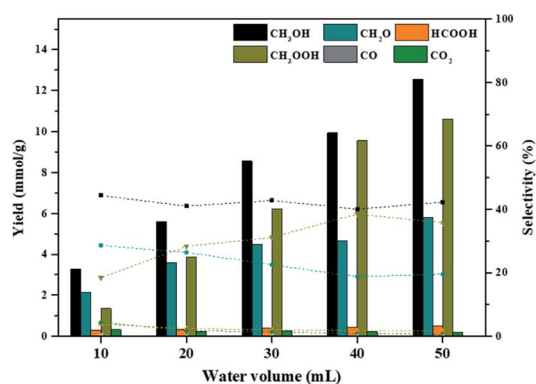


Fig. 8 Photocatalytic methane oxidation over Au–Pd/TiO₂ with different volumes of water under UV-visible light irradiation (5 mg catalyst, 3.0 MPa CH₄, 1.0 MPa O₂, 1 h reaction).

CH₃OOH and CH₂O production, indicating the key role of water as the solvent to remove the oxygenated products from the catalyst surface. Moreover, though the selectivity of CH₃OH remained stable, the selectivity of CH₃OOH increased while that of CH₂O decreased with increasing water volume, suggesting that the dissolution of CH₃OOH in water inhibited its further conversion to CH₂O. However, it should be mentioned that in such a three-phase system containing the catalyst (solid), water (liquid), and CH₄ and O₂ (feed gases), the contact between the catalyst and feed gases can be suppressed by water. Therefore, relatively high pressures of feed gases are desirable, especially for CH₄ whose solubility in water is as low as 22.7 mg L⁻¹ under standard conditions. This was demonstrated by the experimental results; a higher CH₄ pressure led to a higher methane conversion efficiency (Fig. S6†).

Conclusions

In conclusion, an unprecedentedly high efficiency for CH₃OH production was realized, reaching 12.6 mmol g⁻¹ in a one-hour photocatalytic reaction over Au–Pd/TiO₂. This is due to each component in the photocatalytic system. While TiO₂ absorbed UV light to generate electrons and holes, Au–Pd nanoparticles not only helped to transfer photo-generated electrons, but also absorbed visible light to increase the catalyst temperature by ~5 °C. The temperature rise enhanced the driving force for H₂O oxidation into ·OH, O₂ reduction into ·O₂⁻, and more importantly, the reduction of CH₃OOH into CH₃OH. Moreover, by increasing the water volume, the production efficiency could be further enhanced as water could effectively dissolve as-produced oxygenates adsorbed on the catalyst surface. Furthermore, in this case, cost-effective O₂ was surprisingly found to be an even more efficient oxidant than H₂O₂. The above results provide a valuable guide for the design of a photocatalytic system to realize highly efficient conversion of CH₄ to CH₃OH.

Author contributions

Xiaojiao Cai: investigation and validation. Siyuan Fang: investigation and writing – original draft. Yun Hang Hu: conceptualization, supervision, and writing – review & editing.

Conflicts of interest

There are no conflicts to declare.

Notes and references

- 1 X. Cai and Y. H. Hu, *Energy Sci. Eng.*, 2019, 7, 4–29.
- 2 B. Han, W. Wei, L. Chang, P. Cheng and Y. H. Hu, *ACS Catal.*, 2016, 6, 494–497.
- 3 M. Behrens, F. Studt, I. Kasatkin, S. Köhl, M. Hävecker, F. Abild-Pedersen, S. Zander, F. Girgsdies, P. Kurr, B.-L. Kniep, M. Tovar, R. W. Fischer, J. K. Nørskov and R. Schlögl, *Science*, 2012, 336, 893.

- 4 M. M. Konnick, B. G. Hashiguchi, D. Devarajan, N. C. Boaz, T. B. Gunnoe, J. T. Groves, N. Gunsalus, D. H. Ess and R. A. Periana, *Angew. Chem., Int. Ed.*, 2014, **53**, 10490–10494.
- 5 H. Song, X. Meng, S. Wang, W. Zhou, X. Wang, T. Kako and J. Ye, *J. Am. Chem. Soc.*, 2019, **141**, 20507–20515.
- 6 N. Agarwal, S. J. Freakley, R. U. McVicker, S. M. Althahban, N. Dimitratos, Q. He, D. J. Morgan, R. L. Jenkins, D. J. Willock, S. H. Taylor, C. J. Kiely and G. J. Hutchings, *Science*, 2017, **358**, 223.
- 7 V. L. Sushkevich, D. Palagin, M. Ranocchiari and J. A. van Bokhoven, *Science*, 2017, **356**, 523.
- 8 G. J. Hutchings, *Top. Catal.*, 2016, **59**, 658–662.
- 9 X. Meng, X. Cui, N. P. Rajan, L. Yu, D. Deng and X. Bao, *Chem*, 2019, **5**, 2296–2325.
- 10 M. A. Gondal, A. Hameed, Z. H. Yamani and A. Arfaj, *Chem. Phys. Lett.*, 2004, **392**, 372–377.
- 11 S. Murcia-López, K. Villa, T. Andreu and J. R. Morante, *ACS Catal.*, 2014, **4**, 3013–3019.
- 12 W. Zhu, M. Shen, G. Fan, A. Yang, J. R. Meyer, Y. Ou, B. Yin, J. Fortner, M. Foston, Z. Li, Z. Zou and B. Sadler, *ACS Appl. Nano Mater.*, 2018, **1**, 6683–6691.
- 13 K. Villa, S. Murcia-López, T. Andreu and J. R. Morante, *Appl. Catal., B*, 2015, **163**, 150–155.
- 14 J. Xie, R. Jin, A. Li, Y. Bi, Q. Ruan, Y. Deng, Y. Zhang, S. Yao, G. Sankar, D. Ma and J. Tang, *Nat. Catal.*, 2018, **1**, 889–896.
- 15 L. Luo, J. Luo, H. Li, F. Ren, Y. Zhang, A. Liu, W.-X. Li and J. Zeng, *Nat. Commun.*, 2021, **12**, 1218.
- 16 Y. Fan, W. Zhou, X. Qiu, H. Li, Y. Jiang, Z. Sun, D. Han, L. Niu and Z. Tang, *Nature Sustainability*, 2021, DOI: 10.1038/s41893-021-00682-x.
- 17 X. Chen and S. Li, *Chem. Lett.*, 2000, **29**, 314–315.
- 18 S. Fang and Y. H. Hu, *Int. J. Energy Res.*, 2019, **43**, 1082–1098.
- 19 W. Zhou, X. Qiu, Y. Jiang, Y. Fan, S. Wei, D. Han, L. Niu and Z. Tang, *J. Mater. Chem. A*, 2020, **8**, 13277–13284.
- 20 H. Song, X. Meng, S. Wang, W. Zhou, S. Song, T. Kako and J. Ye, *ACS Catal.*, 2020, **10**, 14318–14326.
- 21 A. Hameed, I. M. I. Ismail, M. Aslam and M. A. Gondal, *Appl. Catal., A*, 2014, **470**, 327–335.
- 22 S. W. Verbruggen, M. Keulemans, B. Goris, N. Blommaerts, S. Bals, J. A. Martens and S. Lenaerts, *Appl. Catal., B*, 2016, **188**, 147–153.
- 23 M. Diak, M. Klein, T. Klimczuk, W. Lisowski, H. Remita, A. Zaleska-Medynska and E. Grabowska, *Appl. Catal., B*, 2017, **200**, 56–71.
- 24 H. Tian, S.-Z. Kang, X. Li, L. Qin, M. Ji and J. Mu, *Sol. Energy Mater. Sol. Cells*, 2015, **134**, 309–317.
- 25 X. Tao, L. Shao, R. Wang, H. Xiang and B. Li, *J. Colloid Interface Sci.*, 2019, **541**, 300–311.
- 26 A. Malankowska, M. P. Kobylański, A. Mikolajczyk, O. Cavdar, G. Nowaczyk, M. Jarek, W. Lisowski, M. Michalska, E. Kowalska, B. Ohtani and A. Zaleska-Medynska, *ACS Sustainable Chem. Eng.*, 2018, **6**, 16665–16682.
- 27 Y. Mizukoshi, K. Sato, T. J. Konno and N. Masahashi, *Appl. Catal., B*, 2010, **94**, 248–253.
- 28 R. Su, R. Tiruvalam, A. J. Logsdail, Q. He, C. A. Downing, M. T. Jensen, N. Dimitratos, L. Kesavan, P. P. Wells, R. Bechstein, H. H. Jensen, S. Wendt, C. R. A. Catlow, C. J. Kiely, G. J. Hutchings and F. Besenbacher, *ACS Nano*, 2014, **8**, 3490–3497.
- 29 A. Cybula, J. B. Priebe, M.-M. Pohl, J. W. Sobczak, M. Schneider, A. Zielińska-Jurek, A. Brückner and A. Zaleska, *Appl. Catal., B*, 2014, **152–153**, 202–211.
- 30 P. K. Jain, X. Huang, I. H. El-Sayed and M. A. El-Sayed, *Acc. Chem. Res.*, 2008, **41**, 1578–1586.
- 31 B. Han and Y. H. Hu, *J. Phys. Chem. C*, 2015, **119**, 18927–18934.
- 32 S. Fang, Z. Sun and Y. H. Hu, *ACS Catal.*, 2019, **9**, 5047–5056.
- 33 S. Fang, Y. Liu, Z. Sun, J. Lang, C. Bao and Y. H. Hu, *Appl. Catal., B*, 2020, **278**, 119316.
- 34 C. Wang, S. Fang, S. Xie, Y. Zheng and Y. H. Hu, *J. Mater. Chem. A*, 2020, **8**, 7390–7394.
- 35 X. Wu, J. Lang, Y. Jiang, Y. Lin and Y. H. Hu, *ACS Sustainable Chem. Eng.*, 2019, **7**, 19277–19285.
- 36 B. Han, W. Wei, M. Li, K. Sun and Y. H. Hu, *Chem. Commun.*, 2019, **55**, 7816–7819.
- 37 S. Xie, Y. Liu, J. Deng, S. Zang, Z. Zhang, H. Arandiyan and H. Dai, *Environ. Sci. Technol.*, 2017, **51**, 2271–2279.
- 38 Y. Zhang, Z. Xu, G. Li, X. Huang, W. Hao and Y. Bi, *Angew. Chem., Int. Ed.*, 2019, **58**, 14229–14233.
- 39 X. Chen, L. Liu, P. Y. Yu and S. S. Mao, *Science*, 2011, **331**, 746.
- 40 M. Chen, S. Tang, Z. Guo, X. Wang, S. Mo, X. Huang, G. Liu and N. Zheng, *Adv. Mater.*, 2014, **26**, 8210–8216.
- 41 J. Xiao, J. Rabeah, J. Yang, Y. Xie, H. Cao and A. Brückner, *ACS Catal.*, 2017, **7**, 6198–6206.
- 42 P. K. Sajith, A. Staykov, M. Yoshida, Y. Shiota and K. Yoshizawa, *J. Phys. Chem. C*, 2020, **124**, 13231–13239.
- 43 Y. Nosaka and A. Y. Nosaka, *Chem. Rev.*, 2017, **117**, 11302–11336.
- 44 W. He, H.-K. Kim, W. G. Wamer, D. Melka, J. H. Callahan and J.-J. Yin, *J. Am. Chem. Soc.*, 2014, **136**, 750–757.